Comparative study of electrochemical properties of mixed conducting Ln2NiO4+δ (Ln = La, Pr and Nd) and La0.6Sr0.4Fe0.8Co0.2O3–δ as SOFC cathodes associated to Ce0.9Gd0.1O2–δ, La0.8Sr0.2Ga0.8Mg0.2O3–δ and La9Sr1Si6O26.5 electrolytes

Benoît Philippeau, Fabrice Mauvy, Cécile Mazataud, Sébastien Fourcade, Jean-Claude Grenier

Comparative study of electrochemical properties of mixed conducting $Ln_2NiO_{4+\delta}$ (Ln = La, Pr and Nd) and $La_{0.6}Sr_{0.4}Fe_{0.8}Co_{0.2}O_{3-\delta}$ as SOFC cathodes associated to $Ce_{0.9}Gd_{0.1}O_{2-\delta}$, $La_{0.8}Sr_{0.2}Ga_{0.8}Mg_{0.2}O_{3-\delta}$ and $La_9Sr_1Si_6O_{26.5}$ electrolytes

Benoît Philippeau[a], Fabrice Mauvy[a], Cécile Mazataud[a], Sébastien Fourcade[a], Jean-Claude Grenier[a*]

[a]*CNRS, Université de Bordeaux, ICMCB, 87 avenue du Dr. A. Schweitzer, Pessac F-33608, France*

**Corresponding author. Fax: +33 5 4000 27 61. E-mail address: grenier@icmcb-bordeaux.cnrs.fr (J.-C. Grenier).*

Abstract

The present paper focuses on the comparative study of the electrochemical properties of various mixed conducting oxides used as cathode in alternative couples (cathode/electrolyte) with the aim to improve the performance of the usual couple based on LSM ($La_{0.8}Sr_{0.2}MnO_3$)/YSZ (yttria stabilized zirconia). The oxygen deficient perovskite, $La_{0.6}Sr_{0.4}Fe_{0.8}Co_{0.2}O_{3-\delta}$ (LSFC) and the Ruddlesden–Popper phases, the nickelates $Ln_2NiO_{4+\delta}$ (Ln = La, Pr and Nd) have been investigated as cathode materials for potential application in IT-SOFC systems, using various electrolyte materials such as cerium gadolinium oxide $Ce_{0.9}Gd_{0.1}O_{2-\delta}$ (CGO), substituted lanthanum gallate, $La_{0.8}Sr_{0.2}Ga_{0.8}Mg_{0.2}O_{3-\delta}$ (LSGM) and the apatite-type lanthanum silicate $La_9Sr_1Si_6O_{26.5}$ (LSSO). The chemical reactivity of cathode/electrolyte powder mixtures was investigated by XRD: the results revealed LSFC to have a good chemical compatibility with the various electrolytes while the nickelate oxides showed some reactivity and even a partial decomposition for $Pr_2NiO_{4+\delta}$. The electrochemical properties of these cathode materials have been investigated by impedance spectroscopy under zero dc conditions. The analysis of the impedance diagrams revealed the presence of two processes. The cathodic polarization resistances have been measured and the lowest values at 600 °C are 0.28 and 0.30 $\Omega \cdot cm^2$ for $Pr_2NiO_{4+\delta}/Ce_{0.9}Gd_{0.1}O_{2-\delta}$ and $La_{0.6}Sr_{0.4}Fe_{0.8}Co_{0.2}O_{3-\delta}/La_{0.8}Sr_{0.2}Ga_{0.8}Mg_{0.2}O_{3-\delta}$, respectively. These results have demonstrated that both systems are suitable for IT-SOFC applications.

Keywords : SOFC cathode, Mixed conducting oxides, Lanthanide nickelates, Lanthanum strontium ferro-cobaltite, Electrochemical properties, Cathodic polarization resistance

1. Introduction

In the last few years with the increase of CO_2 emissions, which is the main reason for the global warming, alternative technologies like fuel cells have been considered. Thus, Solid Oxide Fuel Cells (SOFCs) have received much attention because they have a high efficiency and generate low pollution emissions. Nowadays, the use at large scale of (SOFCs) is limited due to their high operating temperatures, typically around 800 °C. Reducing the operating temperature is one of the main challenges for enabling the development of these systems. Currently, the main objective is to decrease the operating temperature to around 600 °C, in order to increase their lifetime and decrease their overall cost (stainless steel instead of ceramics can be used as interconnects, for example). However, two main problems have been identified: one is the lower ionic conductivity of the electrolyte and the other is the higher polarization resistance of the electrodes at reduced temperatures.

In this respect, the use of new electrolytes with high ionic conductivity is required in order to decrease the ohmic loss as well as the development of new cathode materials with MIEC properties, which appears to be a promising way to lower the cathode polarization.

Many oxide ion conductors have been found to be potential candidates as electrolyte for IT-SOFC [1]. Among them, gadolinium-doped ceria is one of the best materials [2]. The substitution of typically 10–20% of the Ce^{4+} ions by trivalent

Gd^{3+} generates oxygen vacancy in the lattice, enabling high oxygen mobility [3]. Doped lanthanum gallate perovskites have been also considered as alternative materials for IT-SOFC [4-5]. $La_{0.8}Sr_{0.2}Ga_{0.8}Mg_{0.2}O_{2.55}$ (LSGM) has been found to exhibit significantly higher oxygen-ion conductivity than conventional YSZ at intermediate temperatures (500–800 °C) and a good chemical stability [6]. Recently, a new family of compounds crystallizing with the apatite-type structure has been also proposed as promising electrolytes because of their good ionic conductivity and their high chemical stability under low oxygen partial pressure $P(O_2)$ [7-8].

Concerning the cathode material, the perovskite-type $AMO_{3-\delta}$ oxide, $La_{1-x}Sr_xFe_{0.8}Co_{0.2}O_{3-\delta}$ (LSFC) has been identified as one of the best oxygen electrodes due to its high catalytic activity for the oxygen reduction reaction (ORR) as well as its excellent ionic and electronic conductivity over a wide temperature range [9]. On the other hand, in attempts to find new materials that can be used as cathodes for IT-SOFC, compounds with K_2NiF_4-type structure, so called Ruddlesden–Popper phases, have been investigated due to their excellent mixed ionic and electronic conducting properties [10-14]. Their general formulation $A_2MO_{4+\delta}$, with M a 3d-transition metal cation and A, a lanthanide or alkaline earth, characterizes some oxygen overstoichiometry and a mixed valence of M in these compounds. Previous studies have shown promising cathode performances with various electrolyte materials, such as yttria stabilized zirconia (YSZ), $Ce_{1-x}Sm_xO_{2-\delta}$ and $La_{1-x}Sr_xGa_{1-y}Mg_yO_{3-\delta}$ (LSGM) [15-17].

In this work, various compositions of mixed ionic–electronic conducting oxide have been selected as cathode materials: the oxygen deficient perovskite $La_{0.6}Sr_{0.4}Fe_{0.8}Co_{0.2}O_{3-\delta}$ and the Ruddlesden–Popper phases, the nickelates $Ln_2NiO_{4+\delta}$ (Ln = La, Pr and Nd) oxides. Their electrochemical properties as IT-SOFC cathodes have been studied using symmetrical cells made with the three electrolytes: $Ce_{0.9}Gd_{0.1}O_{2-\delta}$, $La_{0.8}Sr_{0.2}Ga_{0.8}Mg_{0.2}O_{3-\delta}$ and $La_9Sr_1Si_6O_{26.5}$ (apatite-type compound). The chemical reactivity between the cathodes and the electrolytes was first studied using X-ray diffraction (XRD) analyses. Then, after shaping the electrodes, electrochemical impedance spectroscopy (EIS) measurements were carried out with the aim to identify the various contributions to the polarization resistance as well as the limiting step of the ORR. Post mortem analyses of the cells have been performed in order to examine their microstructure and morphology. The aim of this study is to select the most efficient cathode/electrolyte couple.

2. Experimental

2.1. Preparation of dense electrolytes and porous cathodes

Commercial powders were used as starting materials to prepare dense electrolytes and porous cathodes. Their specifications are listed in Table 1.

Table 1
Powder specifications.

Abbreviation	Composition	Component of the cell	Supplier	$D_{V\,50}$ (μm)
CGO	$Ce_{0.9}Gd_{0.1}O_{2-\delta}$	Electrolyte	Rhodia	0.24
LSGM	$La_{0.8}Sr_{0.2}Ga_{0.8}Mg_{0.2}O_{3-\delta}$	Electrolyte	Fuel Cell Materials	0.72
LSSO	$La_9Sr_1Si_6O_{26.5}$	Electrolyte	ICMCB	0.93
LSFC	$La_{0.6}Sr_{0.4}Fe_{0.8}Co_{0.2}O_{3-\delta}$	Cathode	Marion Technologies	0.27
LAN	$La_2NiO_{4+\delta}$	Cathode	Marion Technologies	0.51
PRN	$Pr_2NiO_{4+\delta}$	Cathode	Marion Technologies	0.49
NDN	$Nd_2NiO_{4+\delta}$	Cathode	Marion Technologies	0.55

D_{V50} is the median size for a volume distribution.

The phase purity was checked by X-ray diffraction (XRD). The data were collected at room temperature over the 2θ angle range 8–80° with a step of 0.02° using a PANalytical X'Pert Pro powder diffractometer in the Bragg–Brentano geometry, using copper K_α radiation.

In order to lower the electrode polarization resistance, an important factor is the particle size of the electrode powders [18]. Actually, a large particle size is disadvantageous to obtaining an important active surface area and conversely, a small particle size leads to increased densification during the sintering step. A good compromise seems to be around 0.50–0.70 µm. In this way, the as-received electrode powders were ball milled. Their particle size distribution was measured with a Malvern Mastersizer 2000 laser granulometer: it is given in Table 1.

In order to obtain dense electrolyte pellets, powders were isostatically pressed at 3000 bars for 15 min and sintered at various temperatures and durations, in air. The preparation conditions for each electrolyte are listed in Table 2. The surface of the pellets was then polished with sandpaper to guarantee uniform surface conditions and finally cleaned with ethanol. All the electrolyte pellets have a diameter of ~ 16 mm, a thickness of ~ 2 mm and a density about 95% of the theoretical value.

Table 2
Conditions for preparing electrolyte ceramics.

Abbreviation	Composition	Supplier	PI (bar/min)	T_S (°C/h)
CGO	$Ce_{0.9}Gd_{0.1}O_{2-\delta}$	Rhodia	3000/15	1400 °C/6 h
LSGM	$La_{0.8}Sr_{0.2}Ga_{0.8}Mg_{0.2}O_{3-\delta}$	Fuel Cell Materials	3000/15	1450 °C/20 h
LSSO	$La_9Sr_1Si_6O_{26.5}$	ICMCB	3000/15	1575 °C/2 h

PI: isostatic pressure; T_S: sintering temperature.

Porous electrodes were made using the screen-printing process. The fine powders were mixed into a solvent with a commercial dispersant (terpineol) and binder (ethylcellulose) to form inks, the formulation of which was optimized to avoid powder agglomeration. Electrodes (of about Ø 15 mm, 1.90 cm^2) were deposited on both sides of the electrolyte pellets by using the semi-automatic screen printer Aurel MOD.C890. A specific high-temperature sintering treatment was required in order to obtain a good adherence between the cathode layer of about 25 µm in thickness and the electrolyte; it is particularly important to get a good quality of the interface while avoiding excessive reaction between materials. The thermal cycle was as follows: an initial ramp at 1 °C min^{-1} up to 400 °C to eliminate organic binders, followed by a temperature increase up to the sintering temperature at 3 °C min^{-1}. With regard to previous works, two sintering conditions were selected: 1100 °C and 1150 °C, for 1 h.

Porosity, adherence and microstructure of the symmetrical cells were checked by field emission scanning electron microscopy (SEM) using a Jeol JSM 6330F equipped with an EDS detector. From cross section of the cell, the cathode layer thickness was measured as well as the porosity calculated by means of image analysis using Image J software.

2.2. Electrochemical measurements

The ionic conductivity of the electrolytes and the polarization resistance of the cathode materials were measured by electrochemical impedance spectroscopy (EIS). These measurements were performed in a two-electrode configuration (under zero dc conditions) on a symmetrical cell, using an Autolab PGSTAT 30 equipped with a frequency response analyzer (FRA), in the range of 0.01 Hz to 1 MHz with a 50 mV signal amplitude. It was checked that in all cases the experimental conditions were in the linear response range of the sample. The complex impedance diagrams were analyzed by means of the Zview™ software (Scribner Associates) using various equivalent circuits constituted of Warburg, Gerisher or R-CPE elements, associated in series [19-23].

3. Results and discussion

3.1. Structural characterization

Structural characterization performed by XRD confirmed that all the materials are single phase. The phase identification was carried out by using the ICCD Database and PANatycal X'Pert Highscore software. Furthermore the refinements were performed with FullProf program to obtain the lattice parameters and space group which are listed in Table 3. These results are in agreement with the literature data [24-26].

Table 3
Cell parameters.

Abbreviation	Composition	Form	Space group	Cell parameters (Å)
CGO	$Ce_{0.9}Gd_{0.1}O_{2-\delta}$	Pellet	Fm-3 m	a = 5.416(7)
LSGM	$La_{0.8}Sr_{0.2}Ga_{0.8}Mg_{0.2}O_{3-\delta}$	Pellet	Pm-3 m	a = 3.919(4)
LSSO	$La_9Sr_1Si_6O_{26.5}$	Pellet	P63	a = 9.705(2); c = 7.211(1)
LSFC	$La_{0.6}Sr_{0.4}Fe_{0.8}Co_{0.2}O_{3-\delta}$	Powder	R-3 c	a = 5.498(6); c = 13.378(6)
LAN	$La_2NiO_{4+\delta}$	Powder	Fmmm	a = 5.467(7); b = 5.462(7); c = 12.693(8)
PRN	$Pr_2NiO_{4+\delta}$	Powder	Fmmm	a = 5.462(7); b = 5.385(5); c = 12.479(1)
NDN	$Nd_2NiO_{4+\delta}$	Powder	Fmmm	a = 5.378(3); b = 5.457(1); c = 12.379(1)

3.2. Chemical reactivity with electrolyte materials

The chemical reactivity between the electrolytes and cathode materials is an important issue for the long-term SOFC performance. It is well known that an excessive reactivity can induce the formation of insulating phases leading to an increase of the polarization resistance and even to drastically lessen the ionic transfer at the cathode/electrolyte interface. On the contrary, a poor cathode adhesion can lead to a smaller contact area and therefore, to a larger interface polarization resistance.

For these reasons, it is important to study the chemical reactivity between the cathode and electrolyte materials in order to optimize the interface. For this purpose, cathode and electrolyte powders were intimately mixed together (1:1 mass ratio) and pressed to form pellets, which exacerbates the reactivity. These pellets were sintered at 1150 °C for 1 h (the same conditions as for the sintering of electrodes (see below)) and aged at 800 °C for 5 days (highest operating temperature). After this thermal treatment, the ground pellets were analyzed by XRD.

3.2.1. Reactivity with CGO

XRD patterns of the LSFC/CGO and NDN/CGO mixtures heated either at 1150 °C for 1 h or at 800 °C for 5 days do not exhibit significant changes: as shown in Fig. 1b,c, all compounds retain their structures. Clearly, no new peaks could be identified in the patterns, indicating that there was no reaction and/or inter-diffusion of elements between cathode and electrolyte. These results reveal that LSFC and NDN have a good chemical compatibility with the CGO electrolyte, which is in agreement with that reported in a previous work [26].

On the other hand, for LAN and PRN, the XRD results reveal that the chemical reactivity with CGO leads to partial or even total decomposition (Fig. 1d, e). After heating at 1150 °C for 1 h, it turned out that LAN is completely decomposed into the high order Ruddlesden–Popper $La_4Ni_3O_{10}$ phase *i.e.* the exsolution of the rare-earth oxides and the oxidation of nickel seem to be enhanced by the presence of CGO. Heated at 800 °C for 5 days, no reactivity is evidenced. This indicates that the reaction should occur after long times of annealing and/or an increase of the temperature. These observations confirm the results reported by Montenegro-Hernandez et al. [27], which suggested the formation of $LaNiO_3$ and $La_4Ni_3O_{10}$ phases after 72 h at 900 °C under air.

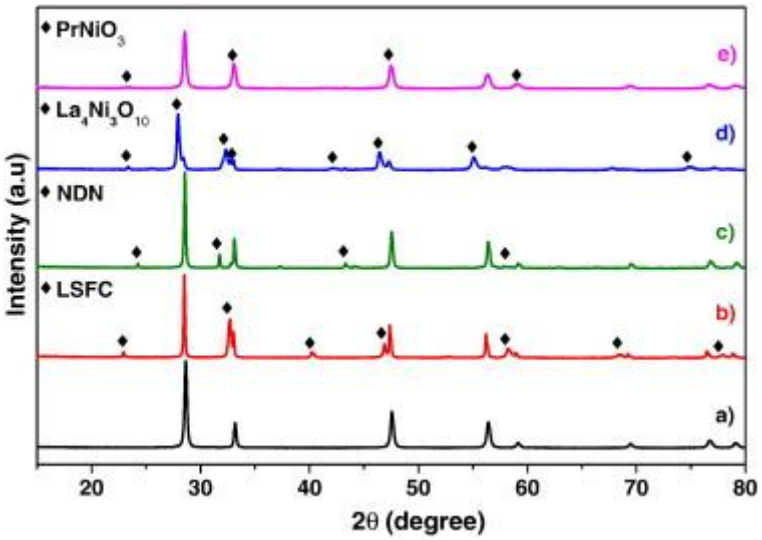

Fig. 1. XRD patterns of: CGO (a) and mixtures of CGO/LSFC (b), CGO/NDN (c), CGO/LAN (d) after heating at 1150 °C for 1 h and PRN/CGO (e) after heating at 800 °C for 5 days.

Concerning PRN, the results given in Table 4 show some reactivity with this electrolyte. After heating at high temperature (1150 °C for 1 h) and at 800 °C for 5 days, it is worth noting that the own decomposition of PRN would take place prior to any reaction between PRN and CGO. However, heated at 800 °C for 5 days, PRN is completely decomposed into a perovskite phase $PrNiO_3$ and traces of nickel oxides are also detected (Fig. 1e). It confirms previous results reported in ref. [27].

Table 4
Results of reactivity experiments in air, for LSFC, LAN, PRN or NDN with CGO electrolyte.

Samples	Reactivity with CGO			
	1150 °C/1 h		800 °C/5 days	
LSFC	/	Stable	/	Stable
LAN	$La_4Ni_3O_{10}$	Total decomposition	/	Stable
PRN	Pr_6O_{11} + ε NiO	Large decomposition (80%)	$PrNiO_3$ + ε NiO	Total decomposition
NDN	/	Stable	/	Stable

Finally, the chemical reactivity between this electrolyte and both LAN, PRN could raise some disadvantage for use as electrode materials.

3.2.2. Reactivity with LSGM

Two kinds of behaviors have been observed with LSGM electrolyte. Concerning LSFC/LSGM as well as LAN/LSGM mixtures, XRD patterns show no significant reaction or decomposition after thermal treatments. However, after sintering at high temperature (1150 °C for 1 h), the presence of small amounts of gallates ($LaSrGa_3O_7$ and $Sr_4Ga_2O_7$) and La_2O_3 can be detected (Fig. 2b, c); they are known to arise from a slight decomposition of LSGM itself during sintering [28-30]. Despite the fact that the fraction of these impurities is small, their very low electrical conductivity and possibly the segregation at the interface electrode/electrolyte could negatively affect the performance of the cell [31]. These observations are in agreement with previous results reported by S.V. Kesapragada et al. [30] and Sayers et al. [32]. Finally, these results reveal that LSFC and LAN have good chemical compatibility with the LSGM electrolyte, which is in agreement with those reported in the literature [33].

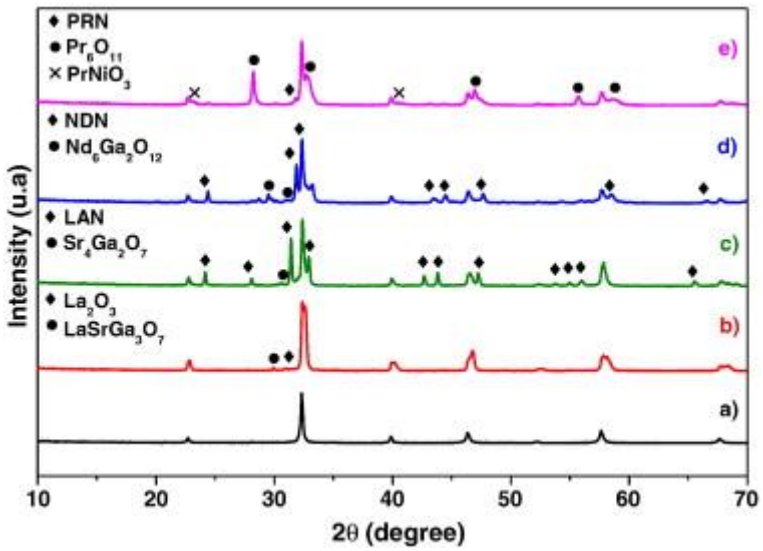

Fig. 2. XRD patterns of: LSGM (a) and mixtures of LSGM/LSFC (b), LSGM/LAN (c) after heating at 1150 °C for 1 h and LSGM/NDN (d), LSGM/PRN (e) after heating at 800 °C for 5 days.

On the other hand, for mixtures of PRN/LSGM and NDN/LSGM, from the results given in Table 5, it should be stressed that both nickelates show some reactivity with this electrolyte. Heated at 1150 °C for 1 h, some amounts of rare-earth gallates besides the Ln_2NiO_4 oxides are evidenced. The formation of these gallates has been assigned by Yamaji et al. to the vaporization of Ga at high temperature and to its high reactivity [34-35]. At 800 °C for 5 days, NDN reacts with LSGM to partially form $Nd_6Ga_2O_{12}$, while PRN is almost completely decomposed into a perovskite phase, $PrNiO_3$-type, and Pr_6O_{11} (Fig. 2d, e). Finally, it can be assumed that the reactivity of these electrode materials with LSGM electrolyte could negatively influence the performances of the LSGM-based cells.

Table 5
Results of reactivity experiments in air, for LSFC, LAN, PRN or NDN with LSGM electrolyte.

Samples	Reactivity with LSGM			
	1150 °C/1 h		800 °C/5 days	
LSFC	$LaSrGa_3O_7$–La_2O_3	Slight decomposition of LSGM (≈5%)	/	Stable
LAN	$Sr_4Ga_2O_7$	Slight decomposition of LSGM (≈3%)	/	Stable
PRN	$Pr_4Ga_2O_9$	Partial reactivity (18%)	$PrNiO_3$–Pr_6O_{11}	8% PRN remains
NDN	$Nd_4Ga_2O_9$	Partial reactivity (18%)	$Nd_6Ga_2O_{12}$	Partial reactivity (14%)

3.2.3. Reactivity with LSSO

Reactivity tests similar to those performed with CGO and LSGM were carried out. Table 6 summarizes the results.

Whatever the thermal treatments, neither reaction nor decomposition could be detected by XRD for LSFC, LAN and NDN materials (Fig. 3b, c, d), which attests to the absence of reactivity with this electrolyte. The results obtained for NDN/LSSO are different from those reported by Porras-Vazquez et al. [36], but agree with those of A. Brisse [37]; the morphology of the powders resulting from the synthesis methods could explain such differences [38].

Table 6
Results of reactivity experiments in air, for LSFC, LAN, PRN or NDN with LSSO electrolyte.

Samples	Reactivity with LSSO			
	1150 °C/1 h		800 °C/5 days	
LSFC	/	Stable	/	Stable
LAN	/		/	
NDN	/		/	
PRN	/		$PrNiO_3$	Partial decomposition (17%)

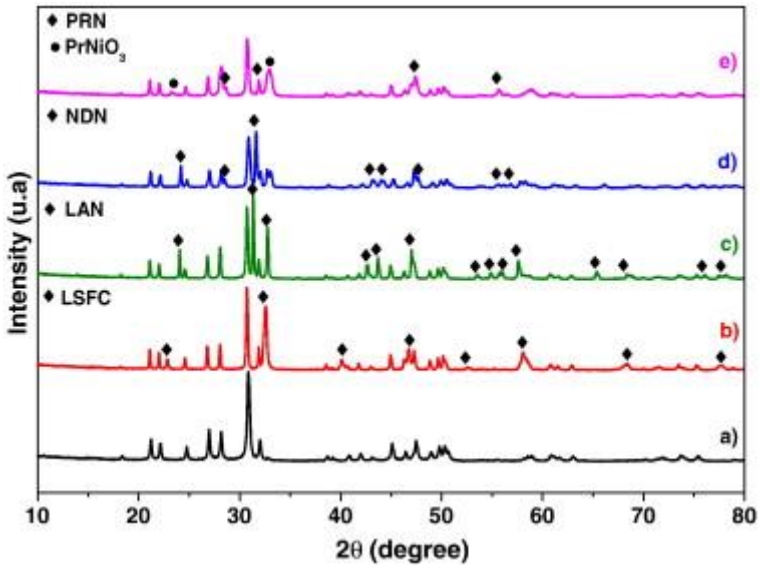

Fig. 3. XRD patterns of LSSO (a), mixture of LSSO/LSFC (b), LSSO/LAN (c), LSSO/NDN (d) after heating at 1150 °C for 1 h and LSSO/PRN (e) after heating at 800 °C for 5 days.

On the other hand, for PRN/LSSO mixture, after 5 days annealing at 800 °C, the diffractogram (Fig. 3e) shows only phases related to the own decomposition of PRN, such as $PrNiO_3$ (●). The absence of other phases seems to indicate that the decomposition of PRN would take place prior to any reaction between PRN and LSSO.

3.3. Ionic conductivity of the electrolytes

In order to control the quality of the as-prepared electrolyte pellets, their ionic conductivity was measured by EIS. Pt-paste electrodes were painted on each side of the pellets as current collectors. The results of ionic conductivity measurements as a function of inverse temperature are reported in Fig. 4. For comparison, the ionic conductivity of the classical 8% yttria-stabilized-ZrO_2 (8YSZ) has been measured on pellet made from Tosoh company powder: the data are also plotted in this figure.

As expected, the ionic conductivity of CGO is the highest one in the studied temperature range, followed by the one of LSGM; 8YSZ and LSSO have similar but lower ionic conductivities. At 700 °C, in air, the values of the ionic conductivity are: 60 mS cm^{-1} for CGO, 42 mS cm^{-1} for LSGM, 25 mS cm^{-1} for 8YSZ and 15 mS cm^{-1} for the LSSO. These values as well as the activation energies well agree with those previously reported in the literature (Fig. 4) [2], [36], [39-42].

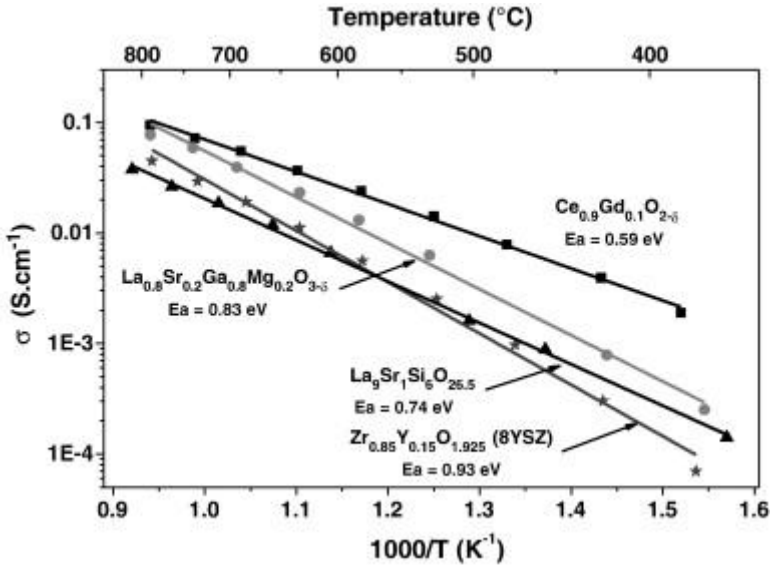

Fig. 4. Arrhenius plots of the ionic conductivity of electrolyte materials, in air.

3.4. Microstructure of the symmetrical cells

In this part, only symmetrical cells sintered at 1150 °C were observed using SEM technique, after impedance measurements in air reported below.

Fig. 5 shows SEM images corresponding to the electrode (≈ 25 µm thick)/CGO interfaces. It can be seen that for LSFC, the microstructure is very different compared to LAN, PRN and NDN. The porosity appears very similar for the nickelate oxides, being close to 30%, while for LSFC it is of the order of only 15%. This observation results probably from the particle size distribution of the starting materials, which is 0.27 µm for LSFC against ≈ 0.50 µm for the nickelate oxides. As previously mentioned, a small particle size seems to favor densification during the sintering step. In addition, it can be noticed that the layers of PRN and LSFC are well connected with the electrolyte ceramic, which characterizes a good interface between both materials.

SEM images of the cross-section of the cathode/LSGM symmetrical cells are reported in Fig. 6. The LSFC electrode is characterized by a smaller grain size and smaller porosity (≈ 20%) compared to nickelate oxide electrodes.

However, all SEM images show good bonding, continuous contact at the interfaces and no delamination between electrode and electrolyte. The thicknesses of the LAN, NDN, PRN and LSFC porous layers were estimated, from the SEM observations, to be approximately 23, 18, 18 and 21 µm respectively.

The SEM micrographs reported in Fig. 7 displays the cross sectional views of the interface between the electrodes and the apatite electrolyte. Each sample shows morphology with porosity of about 30% for LAN and NDN and about 25% for PRN and LSFC, respectively. The thickness of the porous layers varies in the range 14–20 µm. There are no obvious delamination and cracks in the electrode/apatite interfaces, suggesting a good thermal compatibility between the materials. Nevertheless, PRN electrode seems to exhibit the best contact with the dense apatite substrate.

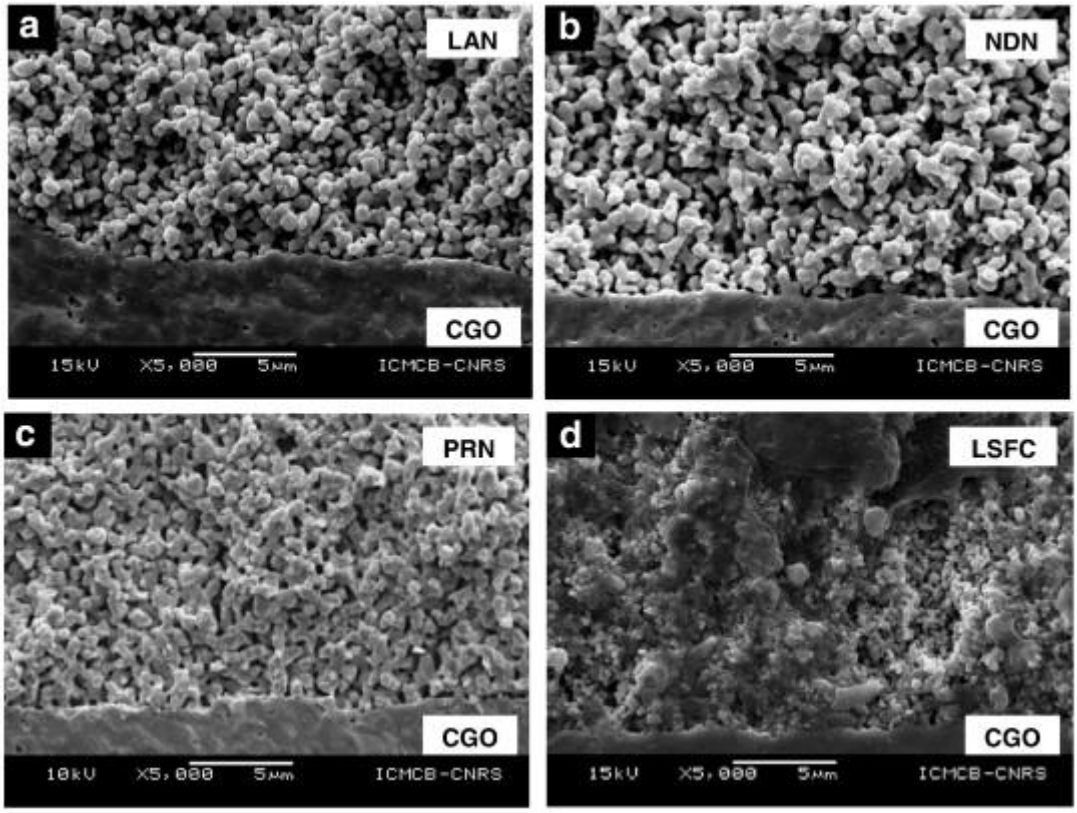

Fig. 5. SEM images of the cross-section of symmetrical cells (cathode/CGO) sintered at 1150 °C, after electrochemical measurements in air.

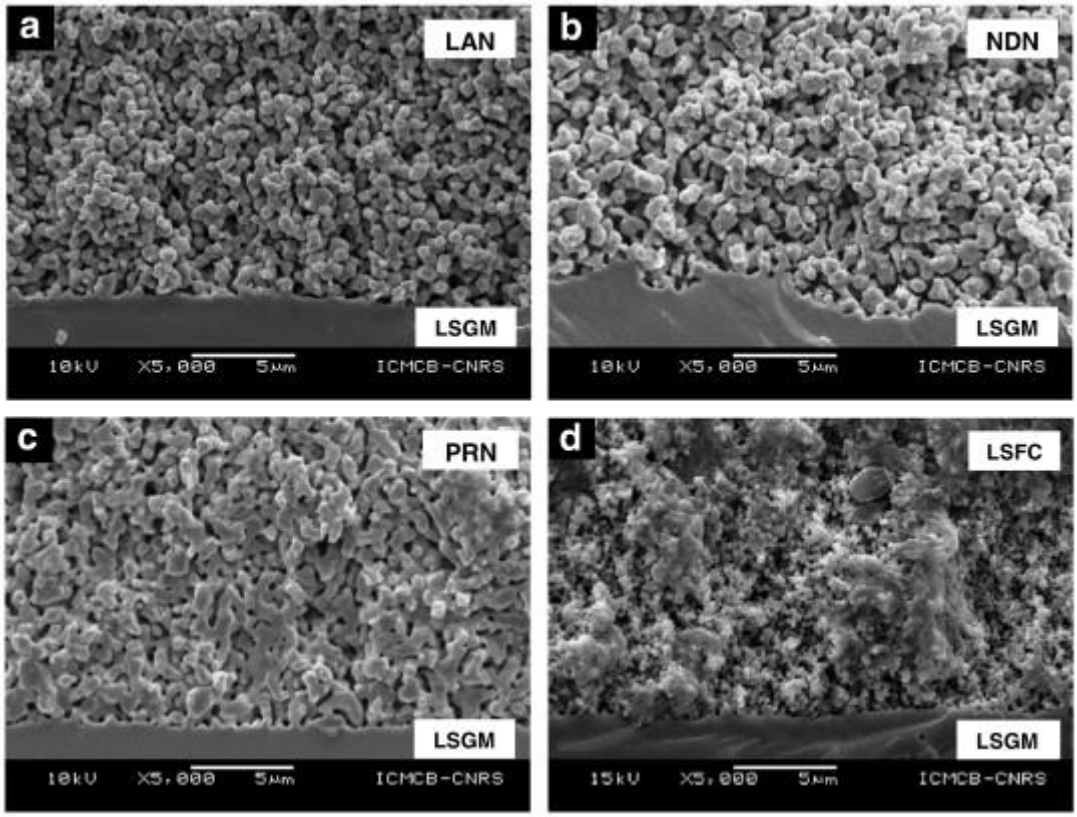

Fig. 6. SEM images of the cross-section of symmetrical cells (cathode/LSGM) sintered at 1150 °C, after electrochemical measurements in air.

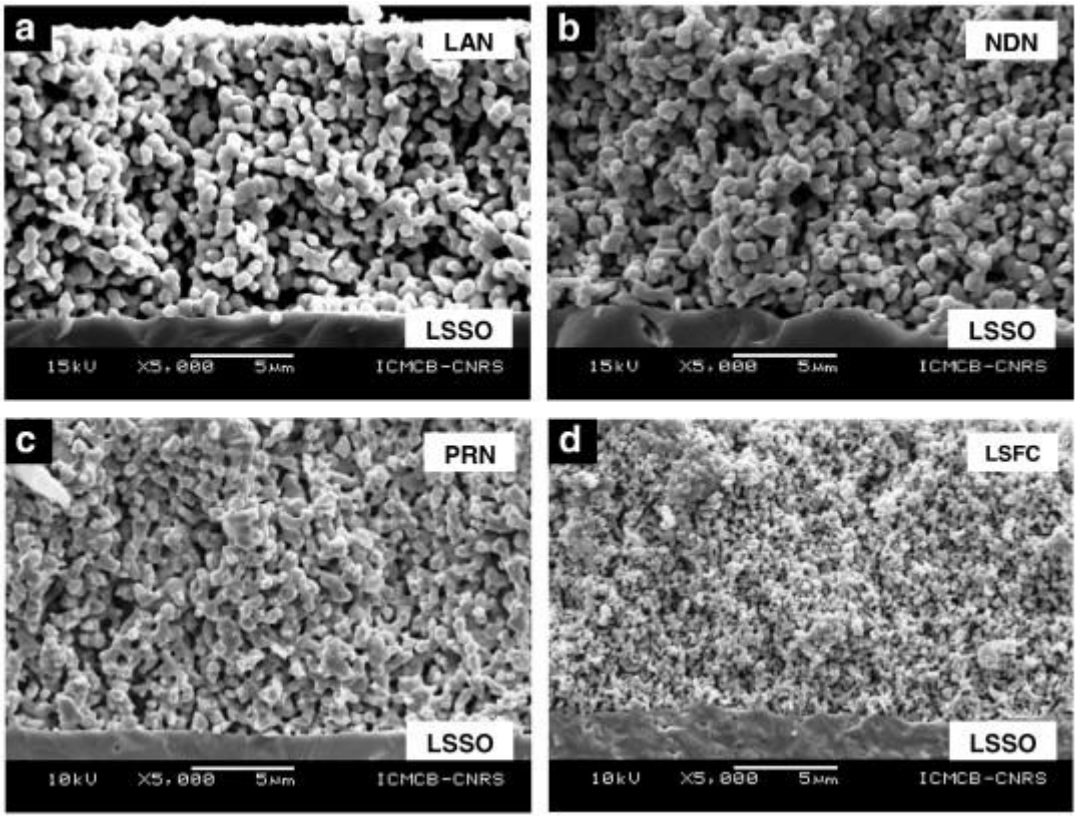

Fig. 7. SEM images of the cross-section of symmetrical cells (cathode/LSSO) sintered at 1150 °C, after electrochemical measurements in air.

3.5. Electrochemical properties under zero dc current conditions

EIS measurements were performed in air, as a function of temperature, at the equilibrium, under zero dc current conditions. A typical Nyquist diagram obtained at 500 °C for $Nd_2NiO_{4+\delta}/Ce_{0.9}Gd_{0.1}O_{1.95}/Nd_2NiO_{4+\delta}$ symmetrical cell, is shown in Fig. 8. Experimental data were fitted using various equivalent circuits: in the high frequency range, the electrolyte was modeled with a series resistance whereas in the middle and low frequency ranges, the polarization resistance of the electrode was fitted using either Warburg-type or Gerisher-type impedance or using an equivalent circuit constituted of several (2 or 3) resistance-constant phase elements, namely R-CPE, in parallel associated in series.

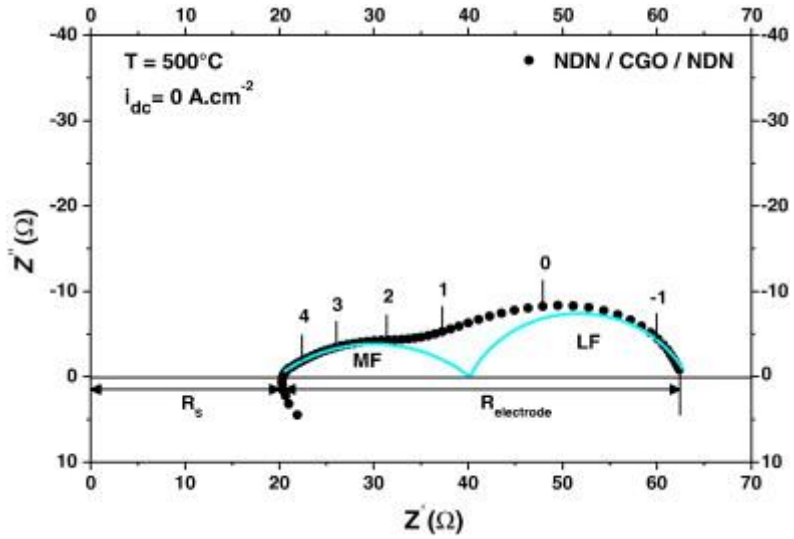

Fig. 8. Typical impedance diagram obtained at T = 500 °C, in air, for a symmetrical cell: NDN/CGO/NDN.

The polarization resistances of the electrode were calculated using the relation $R_p = R_{electrode} \times S/2$, $R_{electrode}$ being the difference between low and high-frequency intercepts of the impedance diagrams with the real axis ($R_{electrode} = R_{MF} + R_{LF}$) and S the surface area of each symmetrical electrode ($S \approx 1.90\ cm^2$).

The electrochemical properties of the ORR at the surface of the cathode materials have been characterized through the polarization resistances of the four selected electrode materials.

3.5.1. Electrochemical properties at $I_{dc} = 0$ with CGO electrolyte

Fig. 9 shows the thermal variation of the polarization resistances of the studied electrode materials sintered on CGO electrolyte at 1150 °C, for 1 h. As expected, R_p decreases with increasing temperature. Table 7 summarizes the values of polarization resistances obtained at 700 °C and 600 °C for these materials. It appears that the values of Rp do not depend significantly on the sintering temperature even though sintering at 1150 °C gives the lowest values.

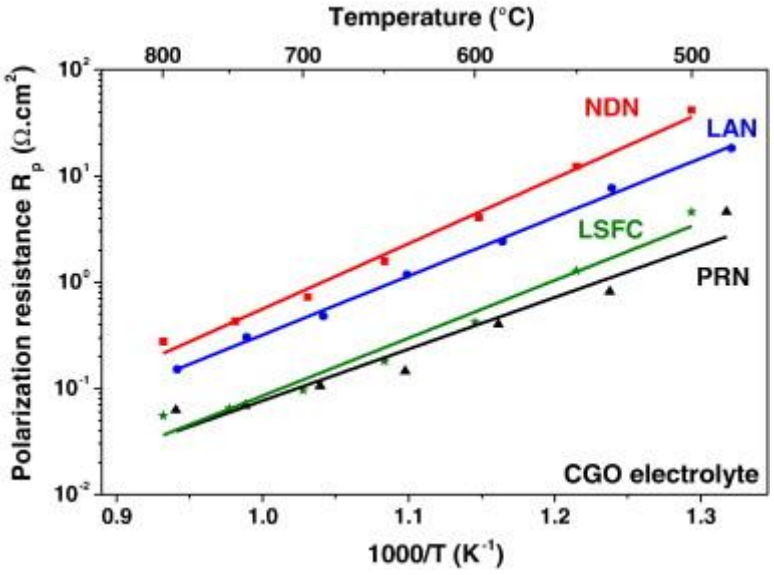

Fig. 9. Arrhenius plots of the polarization resistances for the electrode materials sintered on CGO electrolyte at 1150 °C, for 1 h.

The PRN (in bold in Table 7) and LSFC deposited on CGO electrolyte exhibit the lowest Rp values, 0.12 Ω·cm² and 0.11 Ω·cm² at 700 °C, respectively. These values are comparable to those reported by Kim et al. [43], 0.11 Ω·cm² at 700 °C for the composite electrode, 15%LSFC-GDC, and by Ralph et al. [44], 0.2 Ω·cm² for the single phase electrode LSFC on CGO at the same temperature. These results reveal that the observed metastability of PRN (*cf.* 3.2.1) has no influence on the electrochemical performances. On the other hand, LAN and NDN exhibit the highest Rp values, which can result from the low quality of the interface microstructure between the electrolyte and the cathode layers as seen above.

Table 7
Polarization resistance of the various electrode materials sintered on CGO electrolyte.

Abbreviation	Composition	T_s (°C/h)	Rp (Ω·cm²)	
			700 °C	600 °C
LSFC	$La_{0.6}Sr_{0.4}Fe_{0.8}Co_{0.2}O_{3-\delta}$	1100 °C/1 h	0.14	0.84
LSFC	$La_{0.6}Sr_{0.4}Fe_{0.8}Co_{0.2}O_{3-\delta}$	1150 °C/1 h	0.11	0.42
LAN	$La_2NiO_{4+\delta}$	1100 °C/1 h	0.55	2.2
LAN	$La_2NiO_{4+\delta}$	1150 °C/1 h	0.42	2.0
PRN	**$Pr_2NiO_{4+\delta}$**	**1100 °C/1 h**	**0.12**	**0.28**
PRN	$Pr_2NiO_{4+\delta}$	1150 °C/1 h	0.11	0.36
NDN	$Nd_2NiO_{4+\delta}$	1100 °C/1 h	1.12	4.9
NDN	$Nd_2NiO_{4+\delta}$	1150 °C/1 h	0.72	4.1

3.5.2. Electrochemical properties at I_{dc} = 0 with LSGM electrolyte

The Arrhenius plots of the polarization resistances for the electrode materials sintered on LSGM electrolyte at 1100 °C for 1 h are reported in Fig. 10. The polarization resistance measured for the LSFC electrode clearly evidences the lowest value (in bold in Table 8) whereas NDN electrode shows the highest one over the whole studied temperature range. These values are in agreement with those reported by Lin et al. [45] for the composite electrode 40%LSFC-LSGM 0.06 Ω·cm^2, 0.60 Ω·cm^2 at 700 °C and 600 °C respectively.

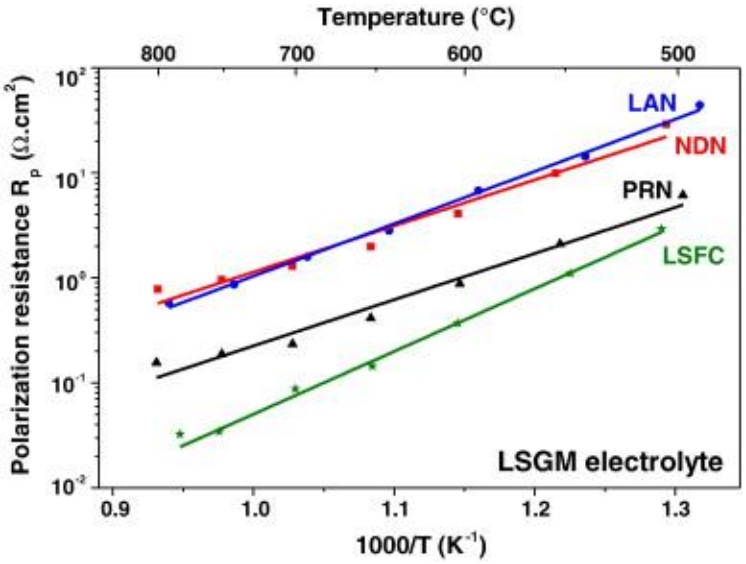

Fig. 10. Arrhenius plots of the polarization resistances for the electrode materials sintered on LSGM electrolyte at 1100 °C for 1 h.

Table 8
Polarization resistance of the various electrode materials sintered on LSGM electrolyte.

Abbreviation	Composition	T_s (°C/h)	Rp (Ω·cm^2)	
			700 °C	600 °C
LSFC	$La_{0.6}Sr_{0.4}Fe_{0.8}Co_{0.2}O_{3-\delta}$	1100 °C/1 h	0.09	0.37
LSFC	**$La_{0.6}Sr_{0.4}Fe_{0.8}Co_{0.2}O_{3-\delta}$**	**1150 °C/1 h**	**0.10**	**0.30**
LAN	$La_2NiO_{4+\delta}$	1100 °C/1 h	1.42	4.5
LAN	$La_2NiO_{4+\delta}$	1150 °C/1 h	1.03	3.7
PRN	$Pr_2NiO_{4+\delta}$	1100 °C/1 h	0.23	0.87
PRN	$Pr_2NiO_{4+\delta}$	1150 °C/1 h	0.33	1.19
NDN	$Nd_2NiO_{4+\delta}$	1100 °C/1 h	1.3	4.1
NDN	$Nd_2NiO_{4+\delta}$	1150 °C/1 h	4.5	17.7

The values of the polarization resistances at 600 and 700 °C are summarized in Table 8. Again, the sintering temperature has no significant effect on the R_P values. However, it seems that a lower sintering temperature leads to the smallest polarization resistances. One can assume that the cathode materials having perovskite-based structures as LSGM would be beneficial for improving the interface and decrease the sintering temperature.

3.5.3. Electrochemical properties at I_{dc} = 0 with LSSO apatite electrolyte

The polarization resistance values obtained for the symmetrical cells sintered at 1100 °C for 1 h on the apatite electrolyte are shown in Fig. 11 as a function of the temperature. The Rp values determined at 700 °C and 600 °C are given in Table 9. Whatever the temperature, the PRN cathode exhibits the lowest R_p (in bold in Table 9) while LSFC shows surprisingly high values (0.16 Ω·cm^2 against ≈ 6 Ω·cm^2 at 700 °C). As no reactivity was detected between LSSO and the cathode materials (*cf.* 3.2.3.), such high values of R_p are assigned to a poor adhesion of LSFC particles on the electrolyte layer (*cf.* Fig. 7). The low values for PRN indicate that the interface polarization has been much improved

compared to the best result reported in the literature for $La_{0.74}Bi_{0.10}Sr_{0.16}MnO_{3+\delta}$ cathode, the polarization resistance of which was 1.38 Ω·cm^2 at 750 °C [46].

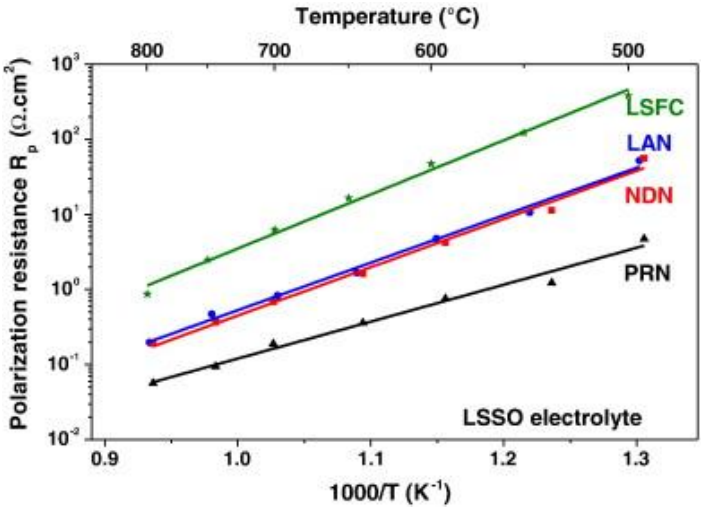

Fig. 11. Arrhenius plots of the polarization resistances for the electrode materials sintered on LSSO electrolyte at 1100 °C for 1 h.

Table 9
Polarization resistance of the various electrode materials sintered on LSSO electrolyte.

Abbreviation	Composition	T_s (°C/h)	Rp (Ω·cm^2)	
			700 °C	600 °C
LSFC	$La_{0.6}Sr_{0.4}Fe_{0.8}Co_{0.2}O_{3-\delta}$	1100 °C/1 h	5.5	39.3
LSFC	$La_{0.6}Sr_{0.4}Fe_{0.8}Co_{0.2}O_{3-\delta}$	1150 °C/1 h	6.4	41.8
LAN	$La_2NiO_{4+\delta}$	1100 °C/1 h	0.79	4.4
LAN	$La_2NiO_{4+\delta}$	1150 °C/1 h	1.73	9.3
PRN	$Pr_2NiO_{4+\delta}$	1100 °C/1 h	0.16	0.62
PRN	**$Pr_2NiO_{4+\delta}$**	**1150 °C/1 h**	**0.16**	**0.55**
NDN	$Nd_2NiO_{4+\delta}$	1100 °C/1 h	0.68	3.8
NDN	$Nd_2NiO_{4+\delta}$	1150 °C/1 h	0.35	2.1

3.6. EIS measurement analysis of selected cathode/electrolyte couples

With respect to the results reported above for CGO, LSGM, and LSSO electrolytes, the three best cathode/electrolyte couples have been selected for further studies. The results obtained by Ogier et al. [47] on YSZ electrolyte have been added for comparison, the EIS measurements having been performed in the same configuration, under zero dc current conditions.

The Arrhenius plots of the polarization resistances for the four symmetrical cells are reported in Fig. 12. With regard to these results, it appears that the lowest R_p values are obtained for the LSFC/LSGM and the PRN/CGO couples. Both half-cells exhibit Rp values close to 0.10 and 0.30 Ω·cm^2, at 700 °C and 600 °C, respectively; these values are in the range of targets required for the development of commercial cells (in bold in Table 7, Table 8).

Nyquist plots obtained at 700 °C for the four symmetrical cells are shown in Fig. 13. For more clarity, the high frequency (HF) contributions of electrolytes have been subtracted. Various types of fitting were performed using different equivalent circuits as quoted above (*cf.* 2.2). No satisfactory fit could be obtained using either the classical Warburg or Gerisher-type impedances, or combinations with R-CPE impedance, which means that the electrode polarization mechanism is more complex. On the other hand, the diagrams were well fitted on the basis of an equivalent circuit constituted of only two R-CPE elements in parallel associated in series, each sub-circuit being represented by a depressed semi-circle in the Nyquist plot.

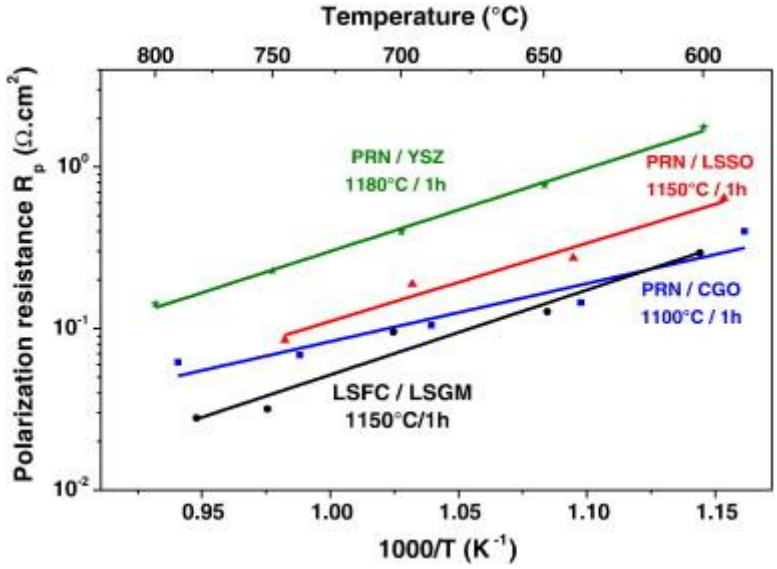

Fig. 12. Arrhenius plots of the polarization resistance for the best symmetrical cells.

Although there is no exact physical meaning behind this equivalent circuit, such a procedure was chosen with regard to the general features of the Nyquist plots as it allows describing the complex response of an electrochemical system. Using the Schouler method [48], resistance and CPE are each assigned to the resistance and capacitance that can be correlated to a specific electrochemical process. On the basis of the fitted data, the frequency relaxation and the equivalent capacitance of each contribution were calculated using relations (1) and (2).

$$f_{relax} = \frac{1}{2\pi(R \times CPE)^{\frac{1}{n}}} \quad (1)$$

$$C_{eq} = R^{\left(\frac{1-n}{n}\right)} \times CPE^{\frac{1}{n}}. \quad (2)$$

The values of the calculated relaxation frequencies (f_{relax}) and equivalent capacitances (C_{eq}) of each impedance contribution have been plotted as a function of the inverse temperature [48-49]. The results are shown in Fig. 14.

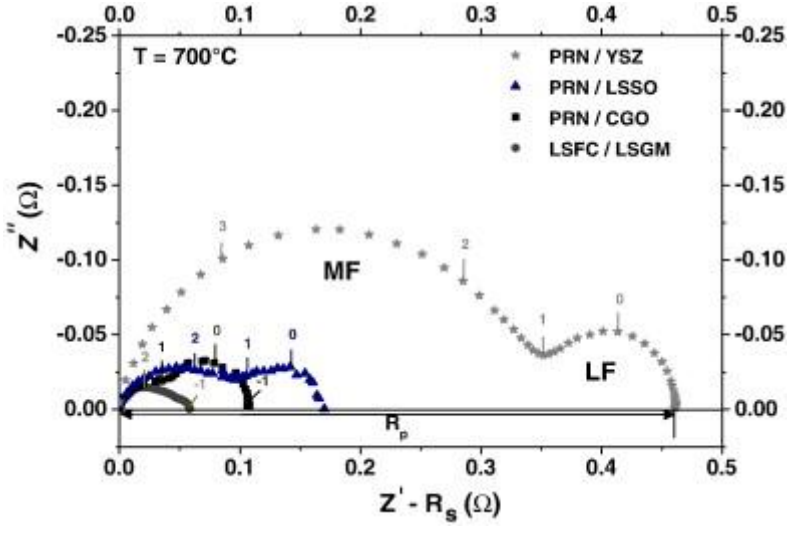

Fig. 13. Nyquist plots obtained at 700 °C with an amplitude of 50 mV for the four cathode/electrolyte couples.

According to the relaxation frequency and the equivalent capacitance values, two domains can be distinguished, at middle frequency (MF) and low frequency (LF), each representing a given electrochemical phenomenon. Nevertheless, the assignment of chemical and/or electrochemical processes is not straightforward.

The low frequency range (LF) is characterized by high capacitance values, $C \approx 1 - 10$ F·cm^{-2}, that are almost independent on temperature, which means the same electrode phenomenon is involved. In recently reported results, L. Mogni et al. [50] and S. Pang et al. [51] have assigned this contribution to the gaseous O_2 diffusion through the porous electrode. However, as this contribution is temperature dependent in our case, the interpretation is more complex and requires additional experiments: it is under investigation [52].

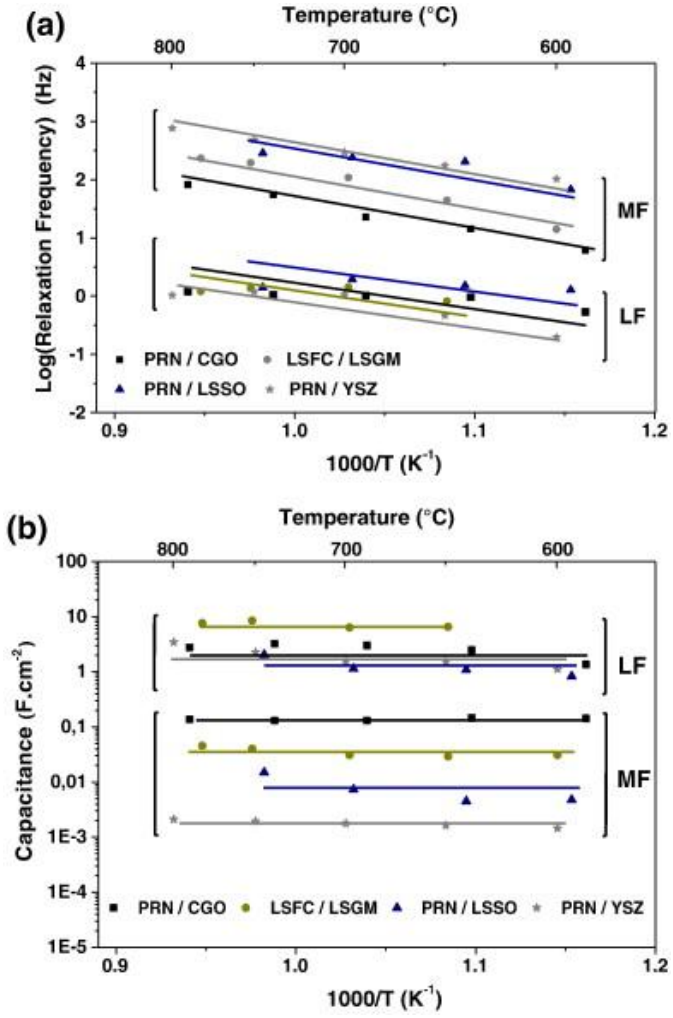

Fig. 14. Arrhenius plots of: (a) the relaxation frequency, (b) the capacitance for the four electrodes.

For the middle frequency contributions (MF), the range of capacitance values is larger, 10^{-1} to 10^{-3} F·cm^{-2}, but is again almost independent on temperature. Impedances located at these frequency and capacitance values have been assigned by previous authors [23], [53-55] to processes of the reaction oxygen reduction (ORR), *i.e.* the molecular oxygen dissociation phenomena and the charge transfer reaction occurring at the electrode/gas interface rather than the ionic transfer at the electrode/electrolyte interface. Experiments as a function of pO_2 would help to assign more precisely this contribution to the EIS diagram [52].

4. Conclusions

Various MIEC oxides have been investigated as cathode materials associated with CGO (doped ceria), LSGM (perovskite-type) and LSSO (apatite-type) electrolytes for potential application in IT-SOFC systems.

The chemical reactivity between the cathode and electrolyte materials has been studied by XRD analyses. Concerning LSFC, the XRD patterns showed no significant reaction with the electrolyte materials. For the nickelates $Ln_2NiO_{4+\delta}$ (Ln = La, Pr and Nd), various behaviors have been observed. In contact with the CGO electrolyte, LAN and PRN are decomposed at 1150 °C. With LSGM electrolyte, a chemical reaction has been observed with PRN and NDN, which might limit the use of these compounds as cathode for IT-SOFC. On the other hand, with LSSO, all materials show no reaction, only PRN undergoes some decomposition at 800 °C, which confirms its metastability in these conditions.

The electrochemical characterizations have been investigated on half-cells made with these different cathode/electrolyte couples. Impedance spectroscopy measurements performed on symmetrical cells (electrode/electrolyte/electrode) under zero dc conditions have allowed determining the polarization resistances of all these cathode materials as a function of temperature. The Rp values show that the couples $Pr_2NiO_{4+\delta}/Ce_{0.9}Gd_{0.1}O_{1.95}$ and $La_{0.6}Sr_{0.4}Fe_{0.8}Co_{0.2}O_{3-\delta}/La_{0.8}Sr_{0.2}Ga_{0.8}Mg_{0.2}O_{2.55}$ exhibit the best properties with values at 600 °C as low as 0.28 and 0.30 $\Omega \cdot cm^2$, respectively. The $Pr_2NiO_{4+\delta}$ decomposition occurring at 800 °C could be avoided if it is used at lower temperatures for the IT-SOFC. Finally, both couples can be considered as suitable for IT-SOFC application.

References

1. V.V. Kharton, F.M.B. Marques, A. Atkinson. Solid State Ionics, 174 (2004), pp. 135-149.
2. B.C.H. Steele. Solid State Ionics, 129 (2000), pp. 95-110.
3. M. Mogensen, Nigel M. Sammesb, Geoff A. Tompsett. Solid State Ionics, 129 (2000), pp. 63-94.
4. K. Huang, R. Tichy, J.B. Goodenough. J. Am. Ceram. Soc., 81 (10) (1998), pp. 2581-2585.
5. K. Huang, J.B. Goodenough. J. Alloys Compd., 454 (2000), pp. 303-304.
6. O. Yamamoto. J. Electrochim. Acta, 45 (2000), pp. 2423-2435.
7. A. Brisse, A.L. Sauvet, C. Barthet, S. Georges, J. Fouletier. Solid State Ionics, 178 (23–24) (2007), pp. 1337-1343.
8. C. Bonhomme, S. Beaudet-Savignat, T. Chartier, P.-M. Geffroy, A.-L. Sauvet. J. Eur. Ceram. Soc., 29 (2009), pp. 1781-1788.
9. L. Qiu, T. Ichikawa, A. Hirano, N. Imanishi, Y. Takeda. Solid State Ionics, 158 (2003), pp. 55-65.
10. E. Boehm, J.-M. Bassat, F. Mauvy, J.-C. Grenier, P. Dordor, A. Watiaux, M. Pouchard. A.J. Mc Evoy (Ed.), Proc. Of the 4th European Solid Oxide Fuel Cell Forum, U. Bossed, Oberrohrdorf, Switzerland (2000), pp. 717-724.
11. S.J. Skinner, J.A. Kilner. Solid State Ionics, 135 (2000), pp. 709-712.
12. E. Boehm, J.-M. Bassat, M.-C. Streil, P. Dordor, F. Mauvy, J.-C. Grenier. Solid State Sci., 5 (2003), pp. 973-981.
13. F. Mauvy, J.-M. Bassat, E. Boehm, J.-P. Manaud, P. Dordor, J.-C. Grenier. Solid State Ionics, 158 (2003), pp. 395-407.
14. F. Mauvy, C. Lalanne, J.-M. Bassat, J.-C. Grenier, H. Zhao, L. Huo, P. Stevens. J. Electrochem. Soc., 153 (2006), pp. 1547-1553.
15. F. Mauvy, C. Lalanne, J.M. Bassat, J.C. Grenier, H. Zhao, P. Dordor, P. Stevens. J. Eur. Ceram. Soc., 25 (2005), pp. 2669-2672.
16. C.N. Munnings, S.J. Skinner, G. Amow, P.S. Whitfield, I.J. Davidson. J. Fuel Cell Sci. Technol., 2 (2005), pp. 34-37.
17. D. Pérez-Coll, A. Aguadero, M.J. Escudero, P. Núñez, L. Daza. J. Power Sources, 178 (2008), pp. 151-162.
18. C. Ferchaud, J.-C. Grenier, Ye Zhang Steenwinkel, Marc M.A. Van Tuel, Frans P.F. van Berkel, J.-M. Bassat. J. Power Sources, 196 (2011), pp. 1872-1879.
19. N. Grunbaum, L. Dessemond, J. Fouletier, F. Prado, A. Caneiro. Solid State Ionics, 177 (2006), pp. 907-913.
20. N. Grunbaum, L. Dessemond, J. Fouletier, F. Prado, L. Mogni, A. Caneiro. Solid State Ionics, 180 (2009), pp. 1448-1452.
21. A. Esquirol, N.P. Brandon, J.A. Kilner, M. Mogensen. J. Electrochem. Soc., 151 (11) (2004), pp. A1847-A1855.

22. V.Ch. Kournoutis, F. Tietz, S. Bebelis. Fuel Cells, 09 (6) (2009), pp. 852-860.
23. M.J. Escudero, A. Aguadero, J.A. Alonso, L. Daza. J. Electroanal. Chem., 611 (2007), pp. 107-116.
24. K. Huang, M. Feng, J.B. Goodenough. J. Am. Ceram. Soc., 81 (1998), pp. 357-362.
25. A. Mineshige, J. Izutsu, M. Nakamara, K. Nigaki, J. Abe, M. Kobune, S. Fujii, T. Yazawa. Solid State Ionics, 176 (2005), pp. 1145-1149.
26. J. Peña-Martínez, D. Marrero-López, C. Sánchez-Bautista, A.J. Dos Santos-García, J.C. Ruiz-Morales, J. Canales-Vazquez, P. Núñez. Bol. Soc. Esp. Ceram., 49 (2010), pp. 15-22.
27. A. Montenegro-Hernandez, J. Vega-Castillo, L. Mogni, A. Caneiro. Int. J. Hydrogen Energy, 36 (2011), pp. 15704-15714.
28. A. Cuneyt Tas, P.J. Majewski, F. Aldinger. J. Am. Ceram. Soc., 83 (12) (2000), pp. 2954-2960.
29. F. Maglia, U. Anselmi-Tamburini, G. Chiodelli, H.E. Camurlu, M. Dapiaggi, Z.A. Munir. Solid State Ionics, 180 (2009), pp. 36-40.
30. S.V. Kesapragada, S.B. Bhaduri, S. Bhaduri, P. Singh. J. Power Sources, 124 (2003), pp. 499-504.
31. M. Rozumek, P. Majewski, H. Schluckwerder, F. Aldinger, K. Kunstler, G. Tomandl. J. Am. Ceram. Soc., 87 (2004), pp. 1795-1798.
32. R. Sayers, J. Liu, B. Rustumji, S. Kinner. J. Fuel Cells, 5 (2008), pp. 338-343.
33. M.-J. Escudero, A. Fuerte, L. Daza. J. Power Sources, 196 (2011), pp. 7245-7250.
34. K. Yamaji, H. Negishi, T. Horita, N. Sakai, H. Yokokawa. Solid State Ionics, 135 (2000), pp. 389-396.
35. W. Kuncewicz-Kupczyk, D. Kobertz, M. Miller, L. Singheiser, K. Hilpert. J. Electrochem. Soc., 148 (2001), pp. E276-E281.
36. J.-M. Porras-Vazquez, L. Dos Santos-Gomez, I. Santacruz, M.A.G. Aranda, D. Marrero-Lopez, E.R. Losilla. Ceram. Int., 38 (2012), pp. 3327-3335.
37. A. Brisse. Thesis of the University Joseph-Fourier Grenoble: Caractérisation électrochimique de matériaux céramiques à microstructure contrôlée pour Piles à Combustible SOFC fonctionnant à température réduite (2006).
38. F.M. Figueiredo, J.A. Labrincha, J.R. Frade, F.M.B. Marques. Solid State Ionics, 101–103 (1997), pp. 343-349.
39. C. Bonhomme, S. Beaudet-Savignat, T. Chartier, A. Maître, A.-L. Sauvet, B. Soulestin. Solid State Ionics, 180 (2009), pp. 1593-1598.
40. Ji-Gui Cheng, Shao-Wu Zha, Jia Huang, Xing-Qin Liu, Guang-Yao Meng. J. Mater. Chem. Phys., 78 (2003), pp. 791-795.
41. R.V. Mangalaraja, S. Ananthakumar, M. Paulraj, K. Uma, M. López, C.P. Camurri, R.E. Avila. Process. Appl. Ceram., 3 (2009), pp. 137-143.
42. T. Fukui, S. Ohara, K. Murata, H. Yoshida, K. Miura. J. Power Sources, 106 (2002), pp. 142-145.
43. J. Hee Kim, H. Kim. J. Ceram. Int., 38 (2012), pp. 4669-4675.
44. J.-M. Ralph, C. Rossignol, R. Kumar. J. Electrochem. Soc., 150 (11) (2003), p. 1518.
45. Y. Lin, S.A. Barnett. Solid State Ionics, 179 (2008), pp. 420-427.
46. J. Zhou, X.F. Ye, J.L. Li, S.R. Wang, T.L. Wen. Solid State Ionics, 201 (2011), pp. 81-86.
47. T. Ogier, F. Chauveau, J.M. Bassat, F. Mauvy, J.C. Grenier, J. Mougin, M. Petitjean. ECS Trans., 35 (1) (2011), pp. 1817-1822.
48. E. Barsoukov, J.R. Macdonald (Eds.), Impedance Spectroscopy (2nd ed.), Wiley-International (2005), p. 87.
49. E.J.L. Schouler, M. Kleitz. J. Electrochem. Soc., 134 (1987), p. 1045.
50. L. Mogni, N. Grunbaum, F. Prado, A. Caneiro. J. Electrochem. Soc., 158 (2) (2011), pp. B202-B207.
51. S. Pang, X. Jiang, X. Li, Q. Wang, Z. Su. J. Power Sources, 204 (2012), pp. 53-59.
52. B. Philippeau, F. Mauvy, C. Nicollet, S. Fourcade, J.-C. Grenier (2013) (submitted for publication to Solid State Ionics).
53. D.J. Chen, R. Ran, K. Zhang, J. Wang, Z.P. Shao. J. Power Sources, 188 (2009), pp. 96-105.
54. W. Zhou, R. Ran, Z. Shao, W. Jin, N. Xu. J. Power Sources, 182 (2008), pp. 24-31.
55. H. Zhao, F. Mauvy, C. Lalanne, J.-M. Bassat, S. Fourcade, J.-C. Grenier. Solid State Ionics, 179 (2008), pp. 2000-2005.